Annual cycle in flow of Ross Ice Shelf, Antarctica: Contribution of variable basal melting

Emilie KLEIN, Cyrille MOSBEUX, Peter D. BROMIRSKI, Laurie PADMAN, Yehuda BOCK, Scott R. SPRINGER, Helen A. FRICKER

Supplementary Material

Table S1. Tidal constituents resolved by T_TIDE and corrected (when marked by a X) from the 2 horizontal time series of stations DR10 (the longest record) and DR05 (a solar-powered station) (section 3.3). Names are provided for the most energetic tides in the vertical component. Constituents marked with * are formally resolved by T_TIDE but not included in tidal corrections for reasons explained in section 3.3. For records shorter than 6 months, including DR05, pairs (S2, K2) and (K1, P1) are resolved by inference.

			DR10		DR05	
Tide	**Period (h)**	**Name**	**North**	**East**	**North**	**East**
S_a	8766.15	Solar annual				
S_{sa}	4382.12	Solar semiannual	*	*		
MSM	763.48					
MM	661.29		X			
MSF	354.37					
MF	327.86					
ALP1	29.07			X		
2Q1	28.01			X		
SIG1	27.85			X		
Q1	26.87	Larger lunar diurnal	X	X	X	X
RHO1	26.72			X		
O1	25.82	Principal lunar diurnal	X	X	X	X
TAU1	25.67		X			
BET1	24.97		X			
NO1	24.83		X	X	X	X
CHI1	24.71			X		
P1	24.07	Principal solar diurnal	X	X	X	X
K1	23.93	Principal lunisolar diurnal	X	X	X	X
PHI1	23.80		X	X		
THE1	23.21		X	X		
J1	23.10		X	X	X	
SO1	22.42		X			
OO1	22.31		X	X		
UPS1	21.58					
OQ2	13.16		X			
EPS2	13.13		X	X	X	X
2N2	12.91		X	X		
MU2	12.87		X	X	X	X
N2	12.66	Larger lunar elliptic semidiurnal	X	X	X	X
NU2	12.63		X	X		

			DR10		DR05	
Tide	**Period (h)**	**Name**	**North**	**East**	**North**	**East**
M2	12.42	Principal lunar semidiurnal	X	X	X	X
MKS2	12.39		X			
LDA2	12.22		X			
L2	12.19		X			
S2	12.00	Principal solar semidiurnal	X	X	X	X
K2	11.97	Declinational lunisolar	X	X	X	X
MSN2	11.79					
ETA2	11.75		X	X	X	X
MO3	8.39		X		X	X
M3	8.28		X		X	X
SO3	8.19		X			
MK3	8.18				X	X
SK3	7.99		X	X	X	X
MN4	6.27		X		X	X
M4	6.21		X		X	X
SN4	6.16		X			
MS4	6.10		X		X	
MK4	6.09		X			
S4	6.00	Shallow water overtides of principal solar	X	X	X	X
SK4	5.99		X			
2MK5	4.93		X		X	
2SK5	4.80		X		X	X
2MN6	4.17		X		X	
M6	4.14		X			
2MS6	4.09					
2MK6	4.09					
2SM6	4.05					X
MSK6	4.04					
3MK7	3.53		X			
M8	3.11				X	

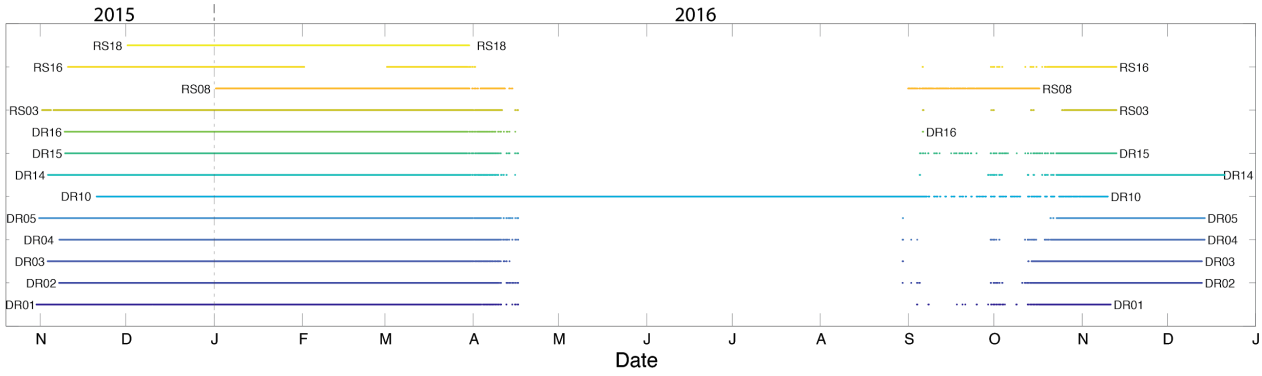

Fig. S1. Data availability at each of our 13 GPS stations on Ross Ice Shelf during 2015-2016.

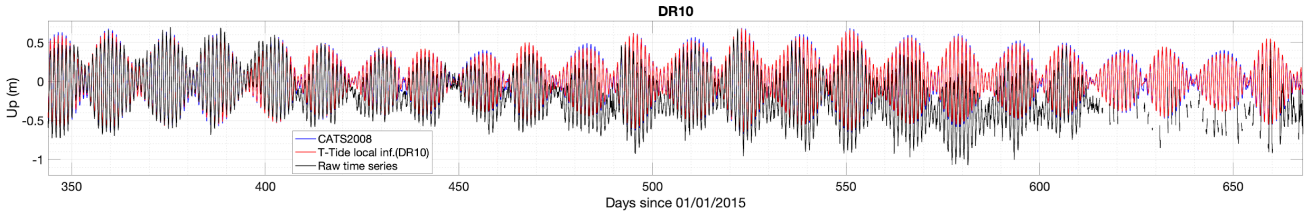

Fig. S2. Raw time series of ice shelf vertical displacement at station DR10 (black curve) compared to CATS2008 prediction (Howard and others, 2019, blue curve) and T_TIDE analysis (red curve). Raw GPS time series show a lowering trend associated with ice thinning and depression of the GPS antenna by surface mass accumulation and compaction of firn underlying the antenna mount.

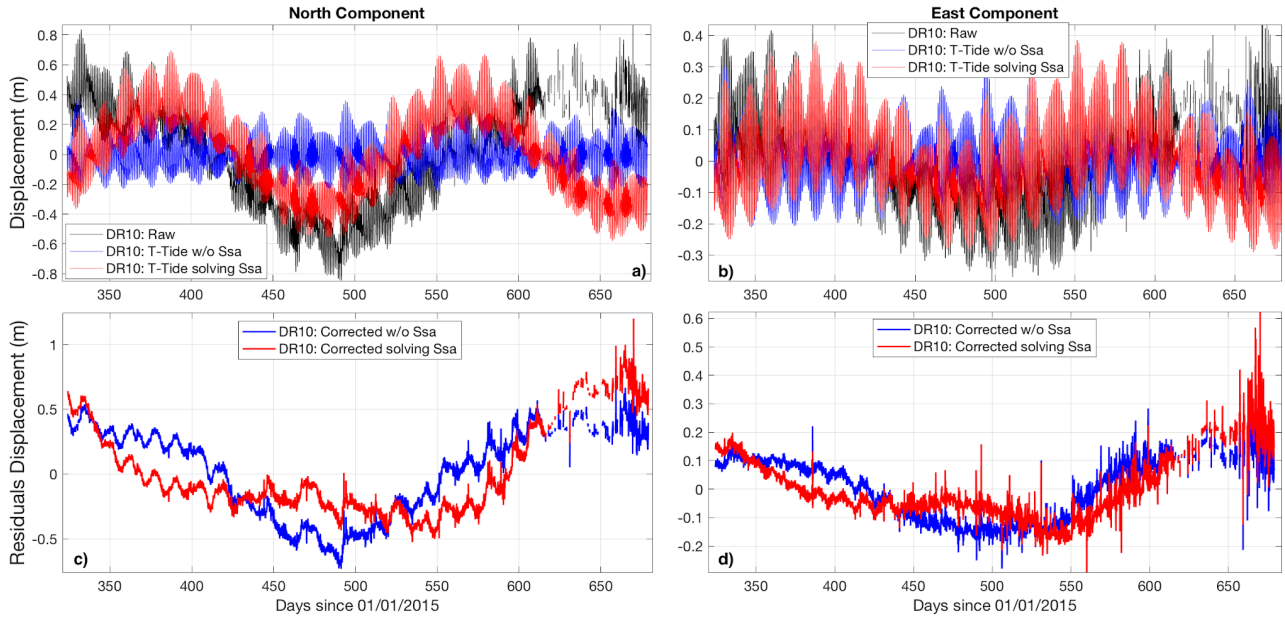

Fig. S3. Horizontal (a) north and (b) east detrended time series of displacements at station DR10 (black) compared to T_TIDE analyses with the solar semi-annual (S_{sa}) signal included (red) and without (blue, same model as in the Main Text). Residuals (c) north and (d) east (observed – T_TIDE analysis) GPS time series for the same station, obtained by removing tidal displacements using T_TIDE estimates in both cases.

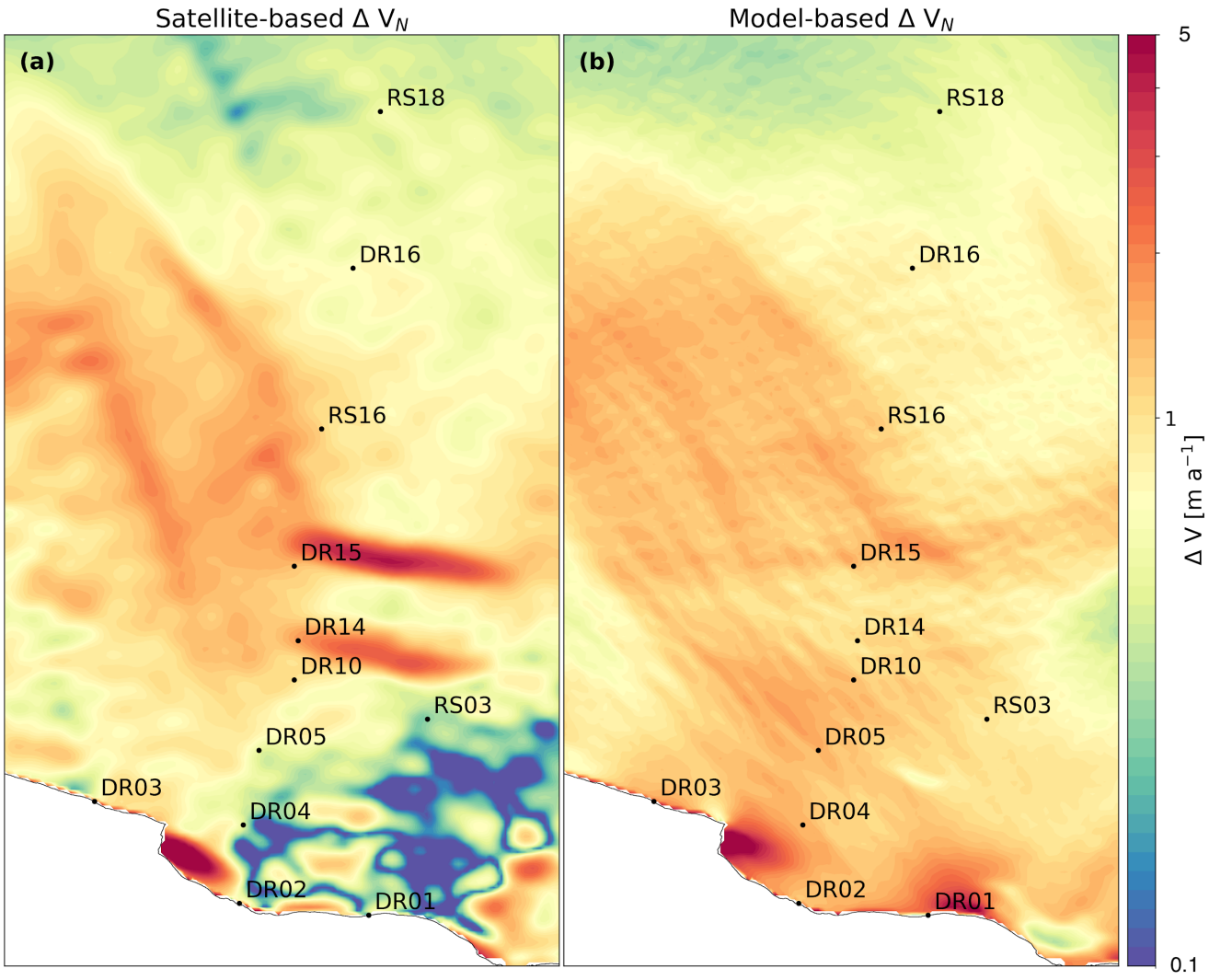

Fig. S4. Change in northward velocity expected after a year of downstream advection based on **(a)** MEaSUREs 20-year average ice velocity field (see section 3.2) smoothed with a 5 km standard deviation Gaussian filter and **(b)** inverse model velocity field (see section 4.2). The MEaSUREs velocity field is affected by the rifts close to DR14 and DR15 as well as potential artefacts (area of high variability) in the polygon defined by DR01, DR02, DR04 and RS03. The model velocity field departs from these potential artefacts and provides a smoother field.

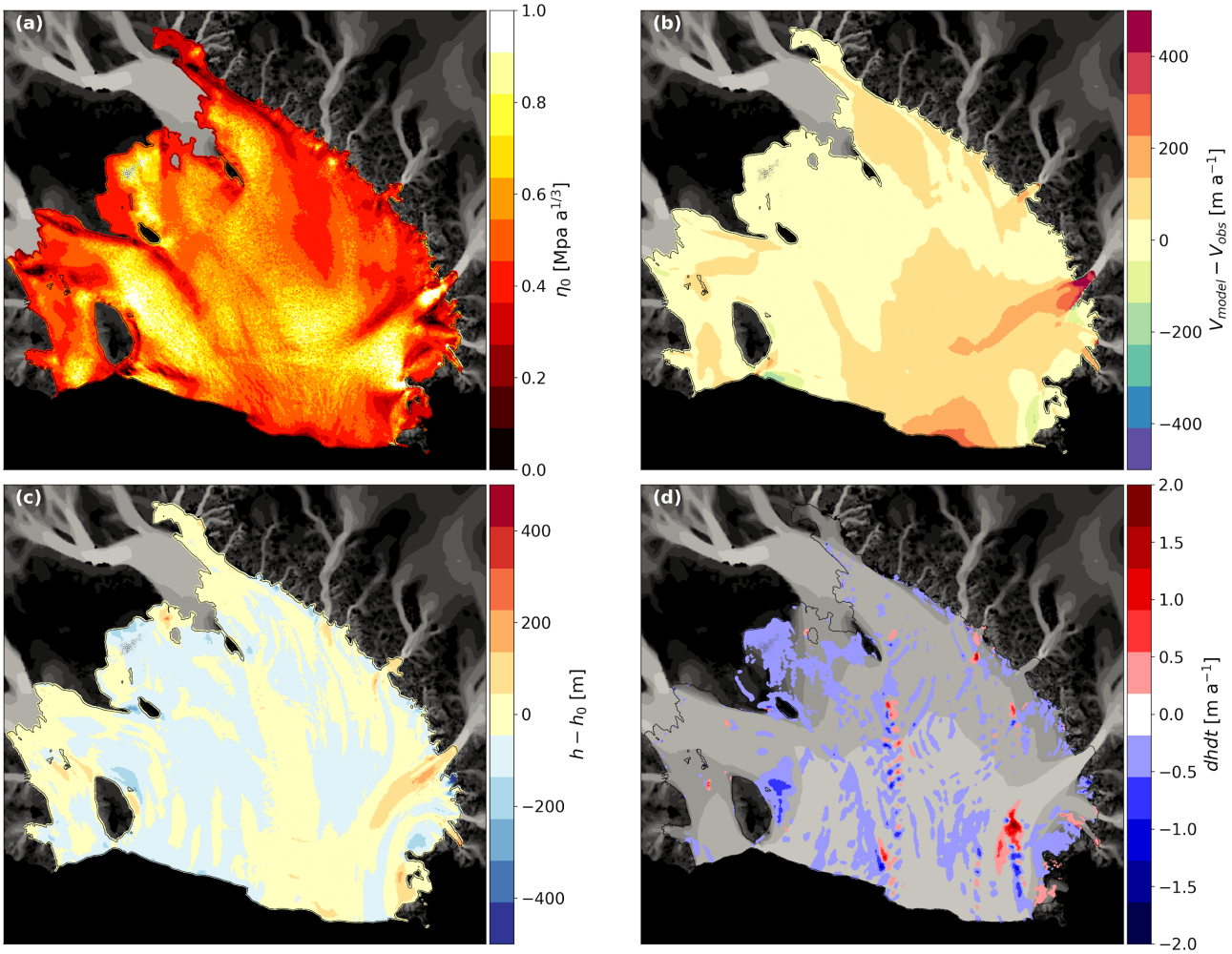

Fig. S5. **(a)** Model inferred viscosity η_0 (MPa $a^{1/3}$) on the ice shelf. Difference between modelled and observed **(b)** velocity and **(c)** ice thickness, after 250 years of relaxation. **(d)** dh/dt at the end of the 250-year relaxation simulation. The background grayscale image represents the model velocity from slow (dark grey) to fast (light grey). The grounding line is plotted as a black line surrounding the ice shelf.

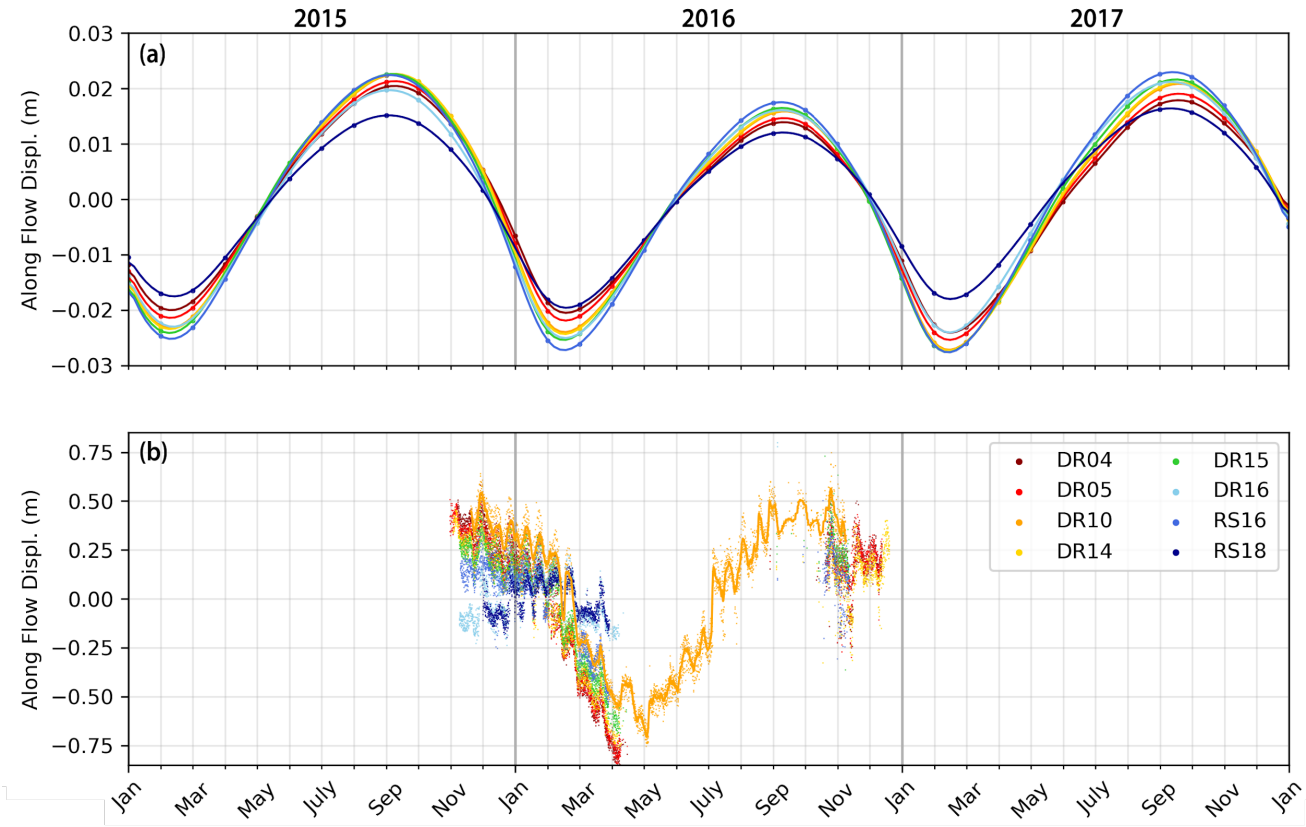

Fig. S6. (a) Modelled and **(b)** observed displacement for different GPS stations (centred on a zero-mean displacement). DR10 observed displacement has been smoothed with a Gaussian filter (with a standard deviation of a day length) and represented with a solid line for a better visualisation of the seasonal variation.

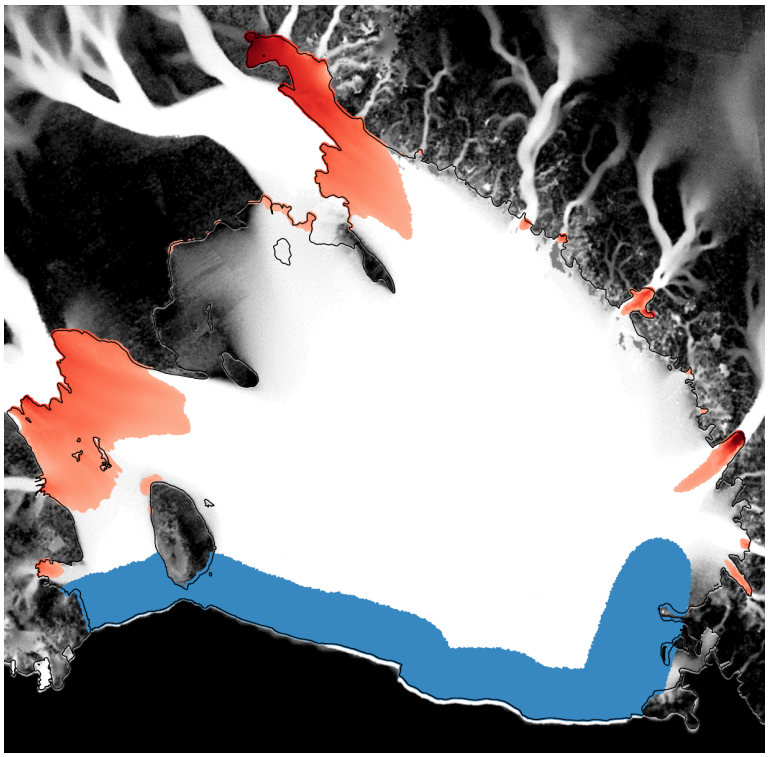

Figure S7. Deep ice base (deeper than 500 below sea level) close to the grounding line (red) and frontal area (blue) where the summer basal melt rate is amplified (by a factor 2 and 3), and/or modified with an extended melt period, for the sensitivity analyses (section 5.2).

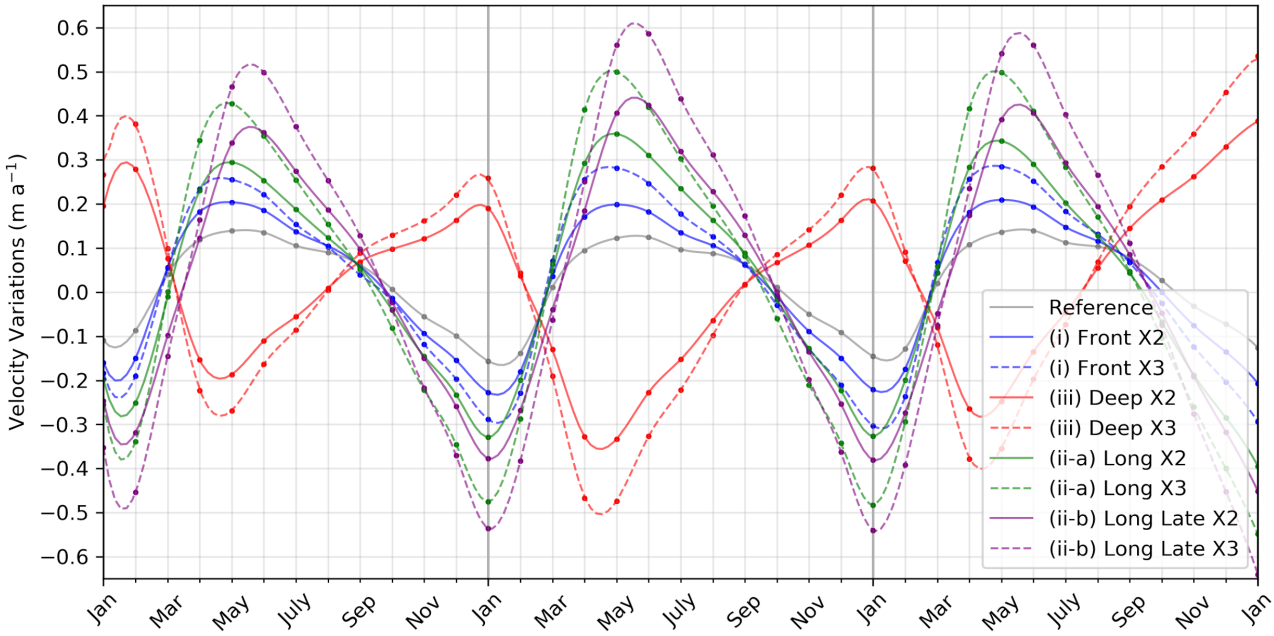

Fig. S8. Sensitivity of the velocity variations to basal melting for DR10; see section 5.2. List of simulations:
(i) frontal melt rate doubled (*Front X2*) and tripled (*Front X3*);
(ii) extended frontal melt periods doubled ((ii-a) *Long X2* and (ii-b) *Long Late X2*) and tripled ((ii-a) *Long X3* and (ii-b) *Long Late X3*);
(iii) deep ice melt doubled (*Deep X2*) and tripled (*Deep X3*). See Fig. S7 for definitions of regions.

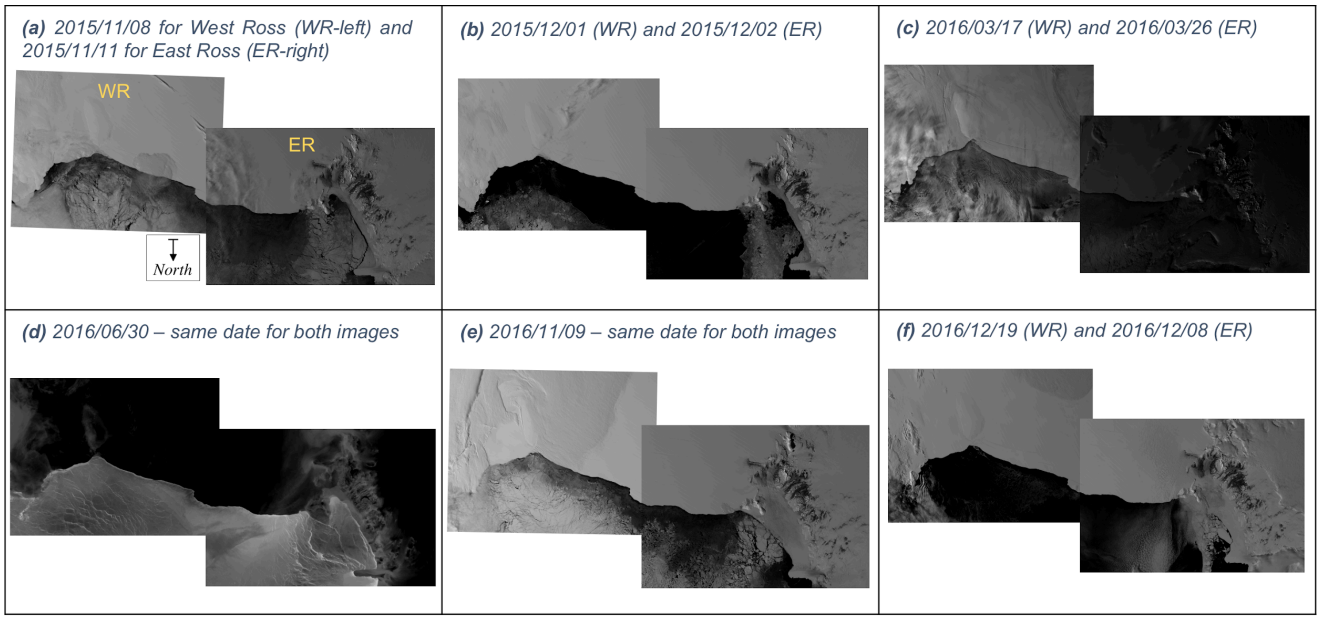

Fig. S9. MODIS images (Scambos and others, 1996) of the RIS ice front at six epochs during the period of operations for the GPS stations. For each epoch, both images (West Ross and East Ross) have been merged, even though they are not always taken at exactly the same time.